



HAL
open science

Ultrafast and persistent photoinduced phase transition at room temperature monitored by streaming powder diffraction

Marius Hervé, Gaël Privault, Elzbieta Trzop, Shintaro Akagi, Yves Watier, Serhane Zerdane, Ievgeniia F Chaban, Ricardo G. Torres Ramírez, Céline Mariette, Alix Volte, et al.

► To cite this version:

Marius Hervé, Gaël Privault, Elzbieta Trzop, Shintaro Akagi, Yves Watier, et al.. Ultrafast and persistent photoinduced phase transition at room temperature monitored by streaming powder diffraction. Nature Communications, 2024, Nature Communications, 15 (1), 10.1038/s41467-023-44440-3 . hal-04431335

HAL Id: hal-04431335

<https://hal.science/hal-04431335>

Submitted on 1 Feb 2024

HAL is a multi-disciplinary open access archive for the deposit and dissemination of scientific research documents, whether they are published or not. The documents may come from teaching and research institutions in France or abroad, or from public or private research centers.

L'archive ouverte pluridisciplinaire **HAL**, est destinée au dépôt et à la diffusion de documents scientifiques de niveau recherche, publiés ou non, émanant des établissements d'enseignement et de recherche français ou étrangers, des laboratoires publics ou privés.

Ultrafast and persistent photoinduced phase transition at room temperature monitored by streaming powder diffraction

Received: 22 June 2023

Accepted: 13 December 2023

Published online: 24 January 2024

Check for updates

Marius Hervé^{1,2}, Gaël Privault^{1,2}, Elzbieta Trzop^{1,2}, Shintaro Akagi³, Yves Watier⁴, Serhane Zerdane⁵, Ievgeniia Chaban^{1,2}, Ricardo G. Torres Ramírez^{1,2}, Celine Mariette^{1,4}, Alix Volte⁴, Marco Cammarata⁴, Matteo Levantino⁴, Hiroko Tokoro^{6,2}✉, Shin-ichi Ohkoshi^{6,2}✉ & Eric Collet^{1,2,7}✉

Ultrafast photoinduced phase transitions at room temperature, driven by a single laser shot and persisting long after stimuli, represent emerging routes for ultrafast control over materials' properties. Time-resolved studies provide fundamental mechanistic insight into far-from-equilibrium electronic and structural dynamics. Here we study the photoinduced phase transformation of the $\text{Rb}_{0.94}\text{Mn}_{0.94}\text{Co}_{0.06}[\text{Fe}(\text{CN})_6]_{0.98}$ material, designed to exhibit a 75 K wide thermal hysteresis around room temperature between $\text{Mn}^{\text{II}}\text{Fe}^{\text{II}}$ tetragonal and $\text{Mn}^{\text{II}}\text{Fe}^{\text{III}}$ cubic phases. We developed a specific powder sample streaming technique to monitor by ultrafast X-ray diffraction the structural and symmetry changes. We show that the photoinduced polarons expand the lattice, while the tetragonal-to-cubic photoinduced phase transition occurs within 100 ps above threshold fluence. These results are rationalized within the framework of the Landau theory of phase transition as an elastically-driven and cooperative process. We foresee broad applications of the streaming powder technique to study non-reversible and ultrafast dynamics.

The ability to control physical properties of materials on demand is an important challenge in science and technology. The use of light as external stimuli, spanning from UV to THz range, is very promising for contact-less, ultrafast and selective control^{1–6}. Ultrashort laser pulses, containing a number of photons of the order of the number of active units within materials, open the way for ultrafast and cooperative switching of their physical properties through photoinduced polarons or lattice instabilities^{7–9}, with various applications for photonic devices or light-based technologies. For optically driven photonic devices, memories, or actuators, the photo-response must combine important

characteristics such as room temperature switching, wide thermal regime of bistability, photoinduced states that can persist long after stimuli, single laser shot with threshold switching and ultrafast dynamics^{10,11}. Molecular materials undergoing photoinduced phase transitions (PIPT) show various types of functionalities switchable under photoexcitation, such as conductivity, ferroelectricity, colour, etc.^{12–20} Among the molecular materials, cyanide-bridged bimetallic assemblies are very attractive compounds exhibiting inter-metallic charge-transfer (CT), which allows for multi-functional properties that can be reversibly controlled by light, including magnetism, ionic

¹Univ Rennes, CNRS, IPR (Institut de Physique de Rennes) - UMR 6251, 35000 Rennes, France. ²CNRS, Univ Rennes, DYNACOM (Dynamical Control of Materials Laboratory) - IRL 2015, The University of Tokyo, 7-3-1 Hongo, Tokyo 113-0033, Japan. ³Department of Materials Science, Faculty of Pure and Applied Sciences, University of Tsukuba, 1-1-1 Tennodai, Tsukuba, Ibaraki 305-8577, Japan. ⁴ESRF - The European Synchrotron, 71 avenue des Martyrs, CS40220, 38043 Grenoble Cedex 9, Grenoble, France. ⁵SwissFEL, Paul Scherrer Institut, Villigen, PSI, Switzerland. ⁶Department of Chemistry, School of Science, The University of Tokyo, 7-3-1 Hongo, Bunkyo-ku, Tokyo 113-0033, Japan. ⁷Institut universitaire de France (IUF), Paris, France. ✉e-mail: tokoro@ims.tsukuba.ac.jp; ohkoshi@chem.s.u-tokyo.ac.jp; eric.collet@univ-rennes.fr

conduction or optical properties such as rotation of light polarization^{21–37}.

Here we present a material of this class, $\text{Rb}_{0.94}\text{Mn}_{0.94}\text{Co}_{0.06}[\text{Fe}(\text{CN})_6]_{0.98}\cdot 0.2\text{H}_2\text{O}$ (hereafter called $\text{RbMn}_{0.94}\text{Co}_{0.06}\text{Fe}$), which exhibits a wide thermal hysteresis centred at room temperature (Supplementary Methods 1) resulting from coupled CT and symmetry-

breaking (SB). We used a streaming powder diffraction technique developed to study its ultrafast and permanent PIPT, induced by a single laser shot at room temperature. The time-resolved X-ray diffraction data show that at low fluence the system remains in a tetragonal and expanded lattice distorted by CT polarons, which are responsible for reverse Jahn–Teller relaxation. Above threshold excitation, the lattice expansion due to photoinduced polarons switches the material from its low-temperature $\text{Mn}^{\text{III}}\text{Fe}^{\text{II}}$ tetragonal ground state to the persistent $\text{Mn}^{\text{II}}\text{Fe}^{\text{III}}$ cubic phase, on the 100 ps timescale. The multiscale nature of the process underlines the key role of elastic interactions in the threshold and cooperative phase transition.

Results

Room-temperature charge-transfer bistability

The synthesized $\text{RbMn}_{0.94}\text{Co}_{0.06}\text{Fe}$ material exhibits a CT-based phase transition similar to the one of the pure $\text{RbMnFe}(\text{CN})_6$ system and derivatives, as characterized by magnetic, X-ray diffraction and infrared measurements (Supplementary Methods 1)³⁸. Figure 1 shows the thermal hysteresis associated with the $\text{Mn}^{\text{II}}\text{Fe}^{\text{III}} \leftrightarrow \text{Mn}^{\text{III}}\text{Fe}^{\text{II}}$ bistability, monitored through the thermal dependence of the $\chi_M T$ product (molar magnetic susceptibility χ_M and temperature T). The $\chi_M T$ value at low temperature (LT) is characteristic of the $\text{Mn}^{\text{III}}(S=2)\text{Fe}^{\text{II}}(S=0)$ state. Upon warming it increases around $T_{\uparrow} = 328\text{ K}$ to reach a value characteristic of the $\text{Mn}^{\text{II}}(S=5/2)\text{Fe}^{\text{III}}(S=1/2)$ high temperature (HT) state. Upon cooling the $\chi_M T$ value suddenly drops back to LT value around $T_{\downarrow} = 253\text{ K}$, resulting in a 75 K wide hysteresis. Compared to the pure $\text{RbMnFe}(\text{CN})_6$ material, for which the thermal hysteresis is centred at 267 K ($T_{\downarrow} = 231\text{ K}$ and $T_{\uparrow} = 304\text{ K}$)³⁸, Co doping allows chemical tuning of the bistability regime, centred at room temperature (290.5 K) for $\text{RbMn}_{0.94}\text{Co}_{0.06}\text{Fe}$. The infrared spectra in the LT and HT phases are characteristic of the $\text{Mn}^{\text{II}}\text{Fe}^{\text{III}}$ and $\text{Mn}^{\text{III}}\text{Fe}^{\text{II}}$ states. Powder X-ray diffraction data show important changes of lattice parameters between the HT cubic space group $F43m$ ($a_{\text{HT}} = 10.5495(6)\text{ \AA}$) and the LT tetragonal space group $F42m$ ($a_{\text{LT}} = 10.0051(11)\text{ \AA}$, $c_{\text{LT}} = 10.4744(16)\text{ \AA}$). This volume contraction between the cubic HT (V_{HT}) and tetragonal LT (V_{LT}) phases corresponds to a large volume strain: $\nu_s = \frac{V_{\text{LT}} - V_{\text{HT}}}{V_{\text{HT}}} \approx -0.1$. The use of the non-conventional $F42m$ LT space group allows for direct description of the symmetry breaking between the two phases, which is due to the collective Jahn–Teller distortion along the z -axis, stabilizing the Mn^{III} LT state. As introduced for RbMnFe ³⁸, the cubic \rightarrow tetragonal symmetry-breaking ferroelastic distortion of the crystalline lattice, due to the loss of the three-fold rotational symmetry, is characterized by its amplitude:

$$\eta(T) = \frac{2}{\sqrt{3}} \left(\frac{c_{\text{LT}}(T) - a_{\text{LT}}(T)}{a_{\text{HT}}} \right) \quad (1)$$

In the framework of the Landau theory of phase transitions³⁸, we have shown that it is also necessary to use a non-symmetry-breaking parameter q to monitor the CT conversion:

$$q = \frac{N_{\text{Mn}^{\text{II}}\text{Fe}^{\text{III}}} - N_{\text{Mn}^{\text{III}}\text{Fe}^{\text{II}}}}{N_{\text{Mn}^{\text{II}}\text{Fe}^{\text{III}}} + N_{\text{Mn}^{\text{III}}\text{Fe}^{\text{II}}}} \quad (2)$$

where $N_{\text{Mn}^{\text{II}}\text{Fe}^{\text{III}}}$ and $N_{\text{Mn}^{\text{III}}\text{Fe}^{\text{II}}}$ denote the number of sites in each CT states. We have shown for similar materials that, during thermal equilibrium phase transitions, the elastic couplings of both parameters q and η to ν_s are responsible for their simultaneous changes from the LT $\text{Mn}^{\text{III}}\text{Fe}^{\text{II}}$ tetragonal ($q = -1$, $\eta \neq 0$) to the HT $\text{Mn}^{\text{II}}\text{Fe}^{\text{III}}$ cubic ($q = 1$, $\eta = 0$) phases and for widening the thermal hysteresis³⁸. As shown in Fig. 1a, the change of electronic state is associated with colour change between $\text{Mn}^{\text{III}}\text{Fe}^{\text{II}}$ tetragonal and $\text{Mn}^{\text{II}}\text{Fe}^{\text{III}}$ cubic states, both stable at room temperature. The LT-to-HT phase transition can also be induced by laser irradiation at room temperature within the thermal hysteresis.

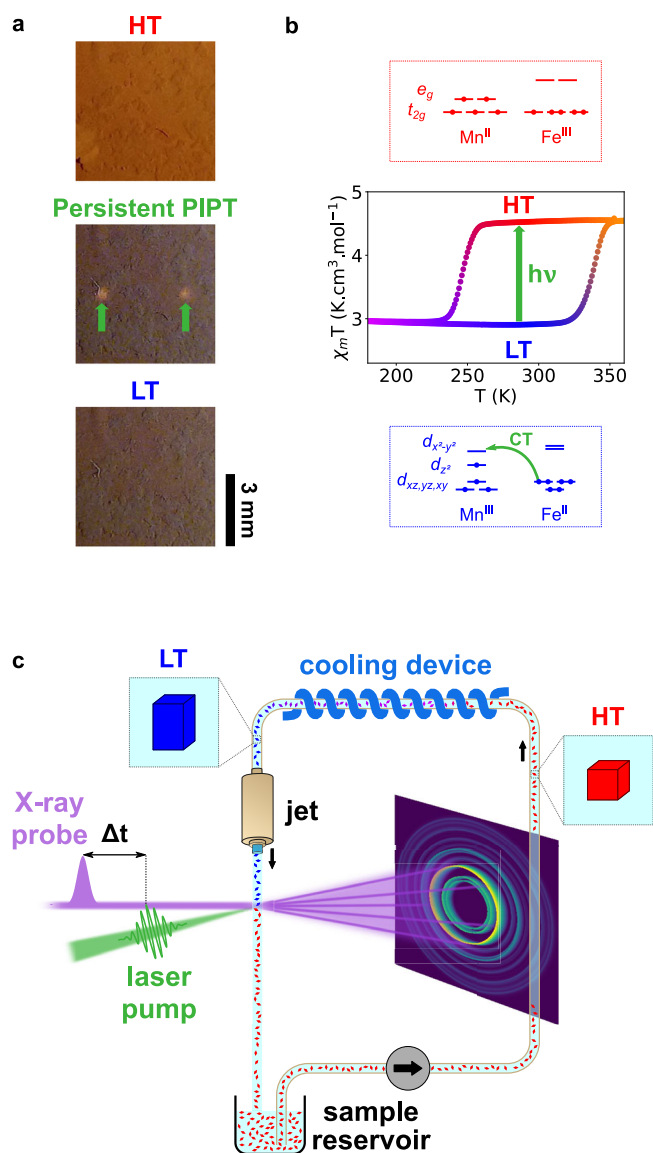


Fig. 1 | Charge-transfer bistability at room temperature. **a** Pictures of $6 \times 6\text{ mm}^2$ $\text{RbMn}_{0.94}\text{Co}_{0.06}\text{Fe}$ thin films taken at room temperature, showing the colour change between the $\text{Mn}^{\text{III}}(S=2)\text{Fe}^{\text{II}}(S=0)$ low-temperature (LT) and $\text{Mn}^{\text{II}}(S=5/2)\text{Fe}^{\text{III}}(S=1/2)$ high-temperature (HT) phases. Starting from the LT phase, a persistent photoinduced phase transition (PIPT) is induced by laser excitation (120 W cm^{-2} , 0.2 mm^2 spot size, 3 s irradiation), as characterized through colour change at laser spot positions (green arrows). Subsequent heating of the irradiated film yields global colour change over the whole film in the HT phase. **b** Thermal hysteresis between the HT and LT phases, characterized through the $\chi_M T$ vs T plot, with the schematic representation of the electronic configurations showing the charge transfer (CT). **c** Streaming powder diffraction technique used for time-resolved measurements, performed on sub- μm crystals of $\text{RbMn}_{0.94}\text{Co}_{0.06}\text{Fe}$ dispersed in solution and streamed through a liquid jet. The X-ray beam probes the sample at a time delay Δt after laser pumping within the hysteresis, which may eventually convert crystals from LT (blue) to permanent HT phase (red). The suspension in the reservoir circulates through a cooling device ($230\text{ K} < T_{\downarrow}$), bringing crystals back to the ground LT phase, before injecting them anew at room temperature in the pump-probe beams.

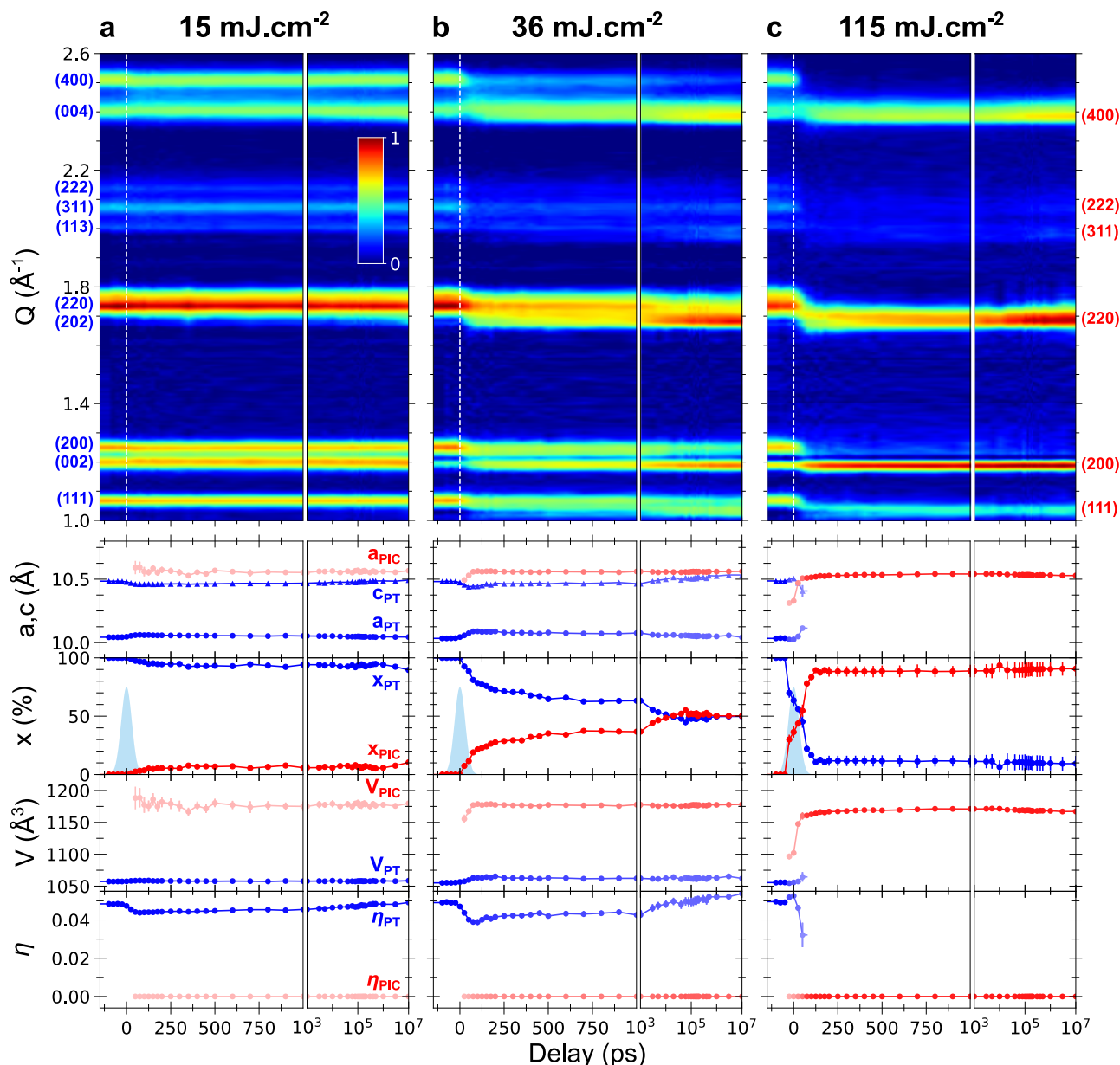


Fig. 2 | Time-resolved X-ray diffraction. Diffracted signal along the scattering vector Q (top) shown with colour-coded intensity and measured at room temperature for low (a, 15 mJ cm^{-2}), medium (b, 36 mJ cm^{-2}) and high (c, 115 mJ cm^{-2}) pumping fluences. The lattice parameters (a , c , V , η) and the fractions of

photoexcited tetragonal (PT, in blue) and photoinduced cubic (PIC, in red) phases are obtained from Rietveld refinement (bottom), and the associated error bars represent the standard deviation of the Rietveld fit for each delay. The time resolution (instrument response function) is shown by the blue Gaussian.

As shown in Fig. 1a, the characteristic colour change occurs at the laser spots, leading to a permanent photoinduced HT phase. In the following, we are interested in understanding the ultrafast out-of-equilibrium dynamics induced by a picosecond laser pulse and driving the $\text{Mn}^{\text{II}}\text{Fe}^{\text{II}}$ tetragonal \rightarrow $\text{Mn}^{\text{II}}\text{Fe}^{\text{III}}$ cubic PIPT within the thermal hysteresis regime of bistability.

Time-resolved crystallography with powder streaming

Understanding the underlying physical mechanisms driving PIPT is mandatory for controlling by light the peculiar properties of these materials. Various ultrafast studies, making use of different techniques, were performed on cyanide-bridged bimetallic assemblies, such as Fe–Fe, Co–Fe, Mn–Fe or V–Cr, and focused on the ultrafast formation of local and transient CT states^{32,34,35,39–43}. In the present work we investigate by streaming powder diffraction (Fig. 1c) the out-of-equilibrium structural dynamics of a macroscopic PIPT in

$\text{RbMn}_{0.94}\text{Co}_{0.06}\text{Fe}$, resulting from a single laser shot excitation within the thermal hysteresis. Conventional time-resolved diffraction techniques consist of exciting a system with a pump pulse and monitoring the change in the X-ray diffraction signal at a given delay Δt ^{6,13,44–48}. Then, the system rapidly recovers the ground state to be excited anew so that stroboscopic pump-probe experiments can be performed at high repetition rates ($>1 \text{ Hz}$) on the same sample. However, this technique cannot be used to study non-reversible phenomena, such as photoswitching within thermal hysteresis. In parallel, serial crystallography, where time-resolved diffraction is performed on fresh single crystals for each laser shot, was largely applied in biology and recently developed for small-unit-cell systems^{49–52}. Regrettably, it cannot be used in the present case because of (i) the limited number of accessible Bragg peaks, given the small cell parameters and high symmetry of $\text{RbMn}_{0.94}\text{Co}_{0.06}\text{Fe}$ and ii) the small size of the crystals giving rise to weak single crystal diffraction. Therefore, we developed a streaming

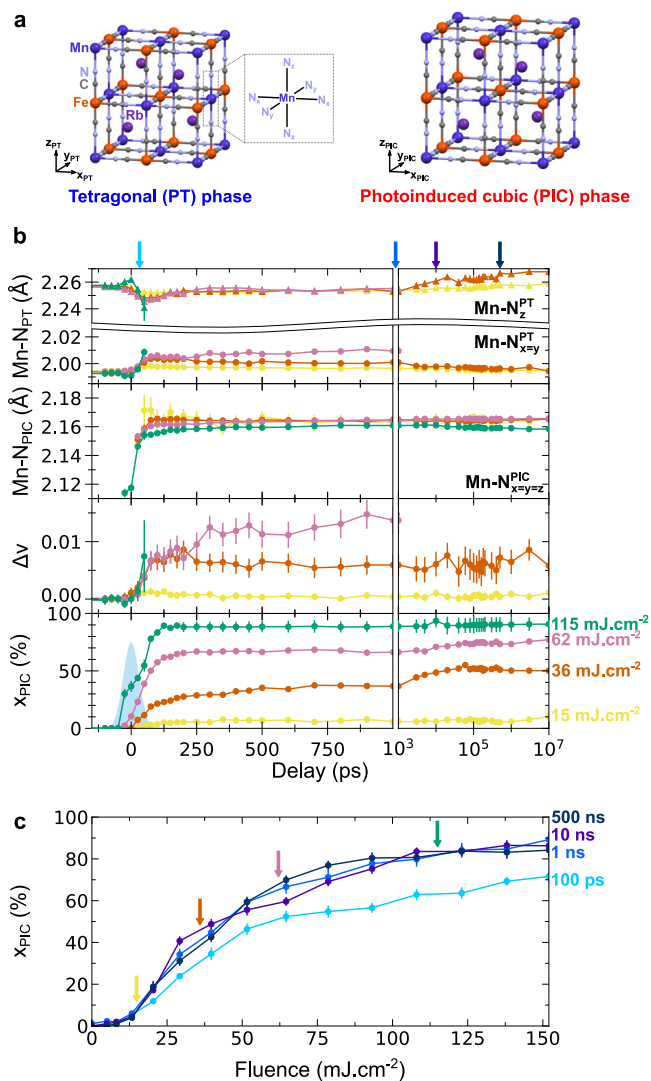


Fig. 3 | Structural reorganizations towards photoinduced cubic phase. a Room temperature photoinduced phase transition from the photoexcited tetragonal (PT) phase to the permanent photoinduced cubic (PIC) phase. **b** Temporal evolution of the Mn–N bond lengths in the PT and PIC phases ($Mn-N_{x=y}^{PT}$, $Mn-N_z^{PT}$, $Mn-N_{x=y=z}^{PIC}$), the relative volume expansion (Δv) of the PT lattice, and the fraction of PIC phase (x_{PIC}) for different laser fluences (yellow: 15 mJ cm⁻², orange: 36 mJ cm⁻², magenta: 62 mJ cm⁻², green: 115 mJ cm⁻²). Reverse Jahn–Teller distortion, Δv and x_{PIC} increase with laser fluence. The time resolution is shown by the blue Gaussian. **c** Fluence dependence of x_{PIC} for different time delays (light blue: 100 ps, blue: 1 ns, purple: 10 ns, dark blue: 500 ns), evidencing threshold fluence for PIPT. The fluences and delays colour codes (arrows and curves) are corresponding between **b** and **c**, and the associated error bars represent the standard deviation of the Rietveld fit for each delay and fluence.

powder diffraction technique (Fig. 1c, Supplementary Methods 2 and 3), which allows for studying out-of-equilibrium photoswitching dynamics inside thermal hysteresis by time-resolved X-ray diffraction (TR-XRD). We used the optical pump–X-ray probe configuration at the ID09 beamline of the European Synchrotron Radiation Facility (ESRF)⁵³ with ~35 ps experimental time resolution. The sample was excited with 1 ps laser pulses. The photoinduced Mn^{II}Fe^{II} → Mn^{III}Fe^{III} CT occurs within 200 fs over a broad excitation spectral range including Fe to Mn CT band (around 500 nm) and Mn-centred band (around 650 nm)³⁰. We excited the sample at 650 nm, which is a good compromise between excitation efficiency and penetration depth (of the order of sample thickness). The typical size of the crystals (0.9 ± 0.3 μm), smaller than the laser pump penetration depth (1.9 μm)⁵⁴, ensures a

relatively homogeneous excitation at the scale of individual crystals dispersed in ethanol (transparent at 650 nm). Streaming powder diffraction experiments consist of performing TR-XRD measurements on a collection of micro-crystals dispersed in solution and streamed through a liquid jet, where they interact with the optical pump and delayed X-ray probe beams, at 1 kHz repetition rate in the present case (Fig. 1c). The overall global fraction of LT crystals exposed to laser shot in the streamed suspension is small. In addition, this suspension circulates through a cooling loop set below T_{\downarrow} , which allows to bring back to the ground LT phase the crystals eventually photoconverted. This ensures that each powder diffraction pattern is measured from a fresh batch of crystals initially in the ground LT state. This closed-loop circulation allows for long data acquisition time, often required in TR-XRD measurements. Both the HT and LT phases were measured at the room temperature of the jet. The lattice parameters of the HT ($a_{HT} = 10.544(2)$ Å) and the LT ($a_{LT} = 10.023(2)$ Å, $c_{LT} = 10.461(2)$ Å) phases, obtained from the Rietveld refinements in the streaming powder diffraction set-up, agree with conventional X-ray powder diffraction data (Supplementary Fig. 7), which shows the quality of the data obtained with streaming powder diffraction. Hereafter we present time-resolved streaming powder diffraction results, which made it possible to track the out-of-equilibrium structural dynamics towards the persistent PIPT, within the thermal hysteresis at room temperature.

Out-of-equilibrium structural dynamics

Figure 2 shows the evolution of the diffraction pattern of RbMn_{0.94}Co_{0.06}Fe crystals, in the initial LT phase, and measured at room temperature as a function of pump-probe delay Δt . We used a Rietveld refinement (Supplementary Methods 4) to track the time evolution of the lattice parameters, phase fractions, and bond lengths for the different phases coming into play. At negative delays, the diffraction pattern corresponds to the initial Mn^{II}Fe^{II} LT phase (F42m space group), where the characteristic Jahn–Teller ferroelastic distortion translates through the splitting of the ($h00$) and ($00h$) Bragg peaks for example. At positive delays, we had to consider two time-dependent phases: a tetragonal phase that describes the evolution of the original phase, called hereafter the photoexcited tetragonal (PT) phase, and a photoinduced cubic (PIC) phase, whose crystalline structure is similar to the HT phase.

Figure 2a shows that for low pumping fluence (15 mJ cm⁻²) the initial LT Bragg peaks shift with delay. The structural Rietveld refinements of the diffraction patterns provide the evolution of the lattice parameters and of the ferroelastic distortion $\eta(t) \propto (c(t) - a(t))/a_{HT}$ for each individual delay t . The lattice parameters of the PT lattice evolve within 100 ps: c_{PT} decreases while $a_{PT} = b_{PT}$ increase, resulting in a global volume increase (1 Å³) and decrease of η . The lattice parameters relax back to initial equilibrium values within 10 μs. Similar lattice distortions were observed at low excitation density under photoexcitation outside thermal hysteresis (below T_{\downarrow}) of the Rb_{0.94}Mn[Fe(CN)₆]·2.5H₂O sample³³. Since RbMnFe and derivative materials exhibit no thermal expansion⁵⁵, it was shown that such long-range lattice deformation results from the structural trapping of photoinduced Mn^{II}Fe^{III} CT state of higher volume, which forms within 200 fs and decays within 10 μs³⁴. At low fluence, the dynamical lattice response therefore includes two components: (i) an impulsive lattice response driven by collective reverse Jahn–Teller reorganizations, elongating a_{PT} and shrinking c_{PT} , and (ii) a volume expansion induced by the long-lived photo-induced CT Mn^{II}Fe^{III} small polarons, populating antibonding Mn $d(x^2 - y^2)$ orbitals. The Rietveld analysis also reveals that a small fraction of photoinduced cubic phase (PIC) appears on the 100 ps timescale ($x_{PIC} \approx 10\%$).

The dynamical behaviour drastically changes when the laser fluence is increased to 115 mJ cm⁻² (Fig. 2c): the diffraction pattern of the initial LT phase almost disappears within 75 ps, while the Bragg peaks of the PIC phase form, characterized by the merging of ($h00$) and

(00*h*) Bragg peaks. Here again, Rietveld refinements enable further understanding of the underlying dynamics at high fluence. After photoexcitation, the lattice parameters a_{PT} and c_{PT} converge within 100 ps towards the cubic lattice parameters. This is due to a larger and global reverse Jahn-Teller distortion, characterized by the fast drop of η for the tetragonal lattice. In addition, the fraction of photoexcited tetragonal phase x_{PT} also drops within 75 ps, while the fraction x_{PIC} of the PIC phase grows rapidly and approaches 100%. Overall, Rietveld analysis shows that high laser fluence drives within 100 ps a global photoinduced Mn^{III}Fe^{II} tetragonal \rightarrow Mn^{II}Fe^{III} cubic phase transition inside the thermal hysteresis and at room temperature. Compared to $V_{LT} = 1055 \text{ \AA}^3$, the volume of the PIC phase increases from $V_{PIC} = 1096(5) \text{ \AA}^3$ within the experimental time resolution to $V_{PIC} = 1167(2) \text{ \AA}^3$ once conversion is complete, which is similar to the volume V_{HT} of the thermodynamically stable HT phase. The remaining fraction of the tetragonal phase is very likely due to the limited laser excitation of crystals in the jet. Interestingly, measurements at intermediate fluence (36 mJ cm^{-2} , Fig. 2b) show a halfway response between low and high excitation densities with intensity decrease and shifts for the PT Bragg peaks and appearance of the PIC ones. Rietveld refinement indicates almost 50% conversion from LT to PIC phases at 36 mJ cm^{-2} , while the fraction of photoexcited sample remaining in the tetragonal lattice exhibits larger reverse Jahn-Teller distortion compared to low fluence. Here again, the tetragonal lattice recovers its initial structure within 10 μs as CT polarons decay, while the fraction of PIC phase is persistent.

Discussion

Figure 3a shows the crystalline structure of the PIC phase, measured at 1 ns and 36 mJ cm^{-2} . The structural data of the PIC phase shown in Supplementary Table 2 are characteristic of the HT Mn^{II}Fe^{III} phase, confirming the occurrence of photoinduced Mn^{III}Fe^{II} tetragonal \rightarrow Mn^{II}Fe^{III} cubic conversion towards the HT phase. To get deeper insights into the PIPT mechanism, we monitored the photo-conversion dynamics as a function of laser fluence, through the temporal evolution of the lattice parameters, $x_{PIC}(t)$ and the relative volume expansion $\Delta v(t) = \frac{V_{PT}(t) - V_{LT}}{V_{HT}}$ of the photoexcited tetragonal lattice at different fluences (Fig. 3b), and through the fluence dependence of $x_{PIC}(t)$ (Fig. 3c). Again, these parameters change within 100 ps. This timescale matches the ratio between crystals' radius (450 nm) and sound velocity ($c = 4300 \text{ m s}^{-1}$ ⁵⁶), which is characteristic of an elastically-driven process^{33,57}. Indeed, since RbMnFe derivatives exhibit no thermal expansion⁵⁵, the initial lattice expansion or ferroelastic distortion cannot be explained by a simple laser heating of the lattice. As can be seen on the evolution of $x_{PIC}(t)$, a second and weaker additional conversion step is observed for intermediate fluences around 10 ns, and is very likely due to slower heat diffusion as observed in spin-crossover materials^{57–59}. Figure 3c shows the fluence-dependent evolution of x_{PIC} at delays of 100 ps, 1, 10 and 500 ns. It clearly evidences a threshold fluence ($\approx 10 \text{ mJ cm}^{-2}$) above which the Mn^{III}Fe^{II} tetragonal \rightarrow Mn^{II}Fe^{III} cubic PIPT is fully established within less than 1 ns.

For fluences below the threshold, Fig. 3b shows that the less bonding photoinduced CT Mn^{II}Fe^{III} state is responsible for Mn-N bond elongations, which translates into the volume expansion Δv of the photoexcited tetragonal lattice. In this polaronic regime, Δv increases with excitation density, while the lattice of the photoexcited crystals retains tetragonal symmetry.

On the other hand, anisotropic lattice distortions in this regime are explained by the anisotropic reorganization around the Mn-N₆ octahedron, as evidenced in Fig. 3b and S7: the structural refinements show elongation of the Mn-N_{x,y} bonds and a contraction of the Mn-N_z ones. This is the direct microscopic evidence of the structural reorganization around the Mn sites from D_{4h} in Mn^{III}Fe^{II} configuration towards O_h for Mn^{II}Fe^{III}. This structural reorganization is characteristic of the reverse Jahn-Teller distortion associated with the photoinduced

CT polarons^{33,34}, which are localized at the level of a single Mn-N-C-Fe unit as previously characterized by time-resolved IR spectroscopy⁴³. This collective local structural dynamics, driven by the photoinduced CT Mn^{II}Fe^{III} polaron, is the driving force of the macroscopic anisotropic lattice deformations: a_{PT} elongates, c_{PT} contracts and therefore η decreases.

Above 10 mJ cm^{-2} , the PIC phase forms within 100 ps and the conversion rate saturates with an almost complete conversion above 100 mJ cm^{-2} . This corresponds to the PIPT regime, with a persistent fraction of the PIC phase. Such a threshold response and fluence dependence are characteristic of cooperative PIPT^{17,57–59}. Together, the ultrafast nature of the phase transformation and its non-linear fluence dependence clearly show that the PIC phase forms through a nucleation process, where a critical fraction of photoinduced CT Mn^{II}Fe^{III} polarons can drive macroscopic PIPT. Since it is hard to estimate precisely the number of absorbed photons, we estimate the percentage of photoexcited units by considering that quantum efficiency is of the order of unity and volume changes linearly with CT fraction^{33,34}. Compared to the relative volume expansion from LT to HT phases ($\Delta v \sim 0.1$) the relative photoexpansion of the PT phase at 62 mJ cm^{-2} ($\Delta v \sim 0.01$, in Fig. 3b) allows us to estimate that 10% of the MnFe units are photoexcited around the excitation threshold.

For each regime, the mechanism at play is deeply related to the evolution of the elastic deformation of the crystals, in particular the volume expansion and the release of the Jahn-Teller distortion. Below threshold excitation, the lattice pressure brings within 10 μs the higher volume photoinduced Mn^{II}Fe^{III} polarons back to their lower volume ground Mn^{III}Fe^{II} state, as characterized by the Mn-N bonds evolution (Fig. 3b). Above threshold, CT polarons drive larger volume expansion, which favours the cubic Mn^{II}Fe^{III} phase of higher volume. Therefore, the overall threshold photoresponse results from the competition between pushing forces of the lattice on the CT polarons, driving their relaxation towards lower volume ground state, and pulling forces of the expanded lattice on ground Mn^{III}Fe^{II} sites, favouring switching towards higher volume Mn^{II}Fe^{III} state.

The role of elastic cooperativity in the present dynamics can be understood within the framework of the Landau theory of phase transition, which we have previously used to describe thermal equilibrium phase transitions in materials exhibiting coupled change of electronic state and symmetry, such as RbMnFe^{38,60,61}. Indeed, the relevant Landau potential should include both the order parameter q monitoring CT and the symmetry-breaking order parameter η (Supplementary Discussion 1). These parameters are coupled to the volume strain v_s . Inside the thermal hysteresis, both the Mn^{II}Fe^{III} cubic phase ($\eta_{HT} = 0$, $q = 1$) and Mn^{III}Fe^{II} tetragonal phase ($\eta_{LT} \neq 0$, $q = -1$) are stable. Hereafter we focus our attention on the more usual Landau potential corresponding to the cubic \rightarrow tetragonal symmetry breaking phase transition^{62–64}:

$$G(\eta) = \frac{1}{2} a' \eta^2 + \frac{1}{3} b \eta^3 + \frac{1}{4} c \eta^4 \quad (3)$$

where the renormalized coefficient $a' = a + 2\lambda_\eta v_s$ includes both the usual temperature-induced symmetry-breaking term ($a = a_0(T - T_{SB})$) and the elastic coupling of the ferroelastic distortion to v_s ($v_s \eta^2 < 0$) where $v_s < 0$ stabilizes the tetragonal phase^{65,66}. a changes sign at the symmetry-breaking temperature T_{SB} , which stabilizes $\eta = 0$ above T_{SB} and $\eta \neq 0$ below, while the symmetry-allowed η^3 term limits the $F\bar{4}3m \rightarrow F\bar{4}2m$ ferroelastic transition to first-order. Inside the thermal hysteresis, both the high-volume cubic phase ($\eta_{HT} = 0$, $v_s = 0$) and low-volume tetragonal phase ($\eta_{LT} \neq 0$, $v_s < 0$) are stable, due to the elastic coupling to v_s of the ferroelastic distortion η . Figure 4 shows the $G(\eta)$ curve obtained from Eq. (3) when cubic and tetragonal phases are equally stable (left panel). To describe the lattice response to photoexcitation, we should consider the results from the

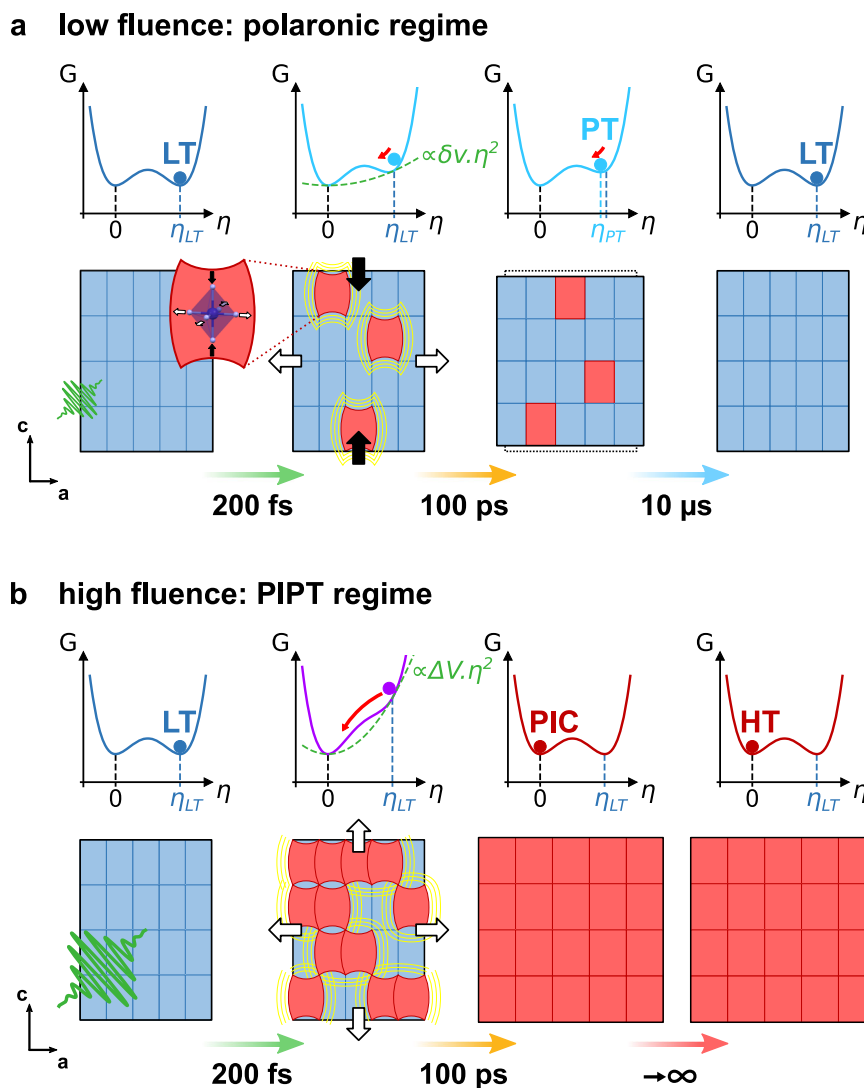


Fig. 4 | From local charge-transfer polarons to macroscopic photoinduced phase transition driven by lattice expansion. **a** Transient polaronic regime at low fluence inside thermal hysteresis, where $G(\eta)$ corresponds to equally stable low-temperature (LT, $\eta_{LT} \neq 0$) and high-temperature (HT, $\eta_{HT} = 0$) phases (dark blue curve). Excitation of the tetragonal $\text{Mn}^{\text{III}}\text{Fe}^{\text{II}}$ ground state results in charge-transfer (CT) polarons (represented as red sites in the crystal) responsible for a weak volume expansion δv . The additional elastic coupling cost $\propto \delta v \eta^2$ (dashed green curve) reduces the amplitude of the ferroelastic distortion, which equilibrates on elastic timescale (100 ps) to η_{PT} in the photoexcited tetragonal (PT) lattice (light

blue curve). As CT polarons, and therefore δv , decay within 10 μs , the system relaxes towards the initial ground $\text{Mn}^{\text{III}}\text{Fe}^{\text{II}}$ state (dark blue curve). **b** Persistent photoinduced phase transition (PIPT) regime at high fluence, where the larger volume expansion ΔV strongly destabilizes the tetragonal lattice within 100 ps (purple curve), converting crystals towards the photoinduced cubic phase (PIC, $\eta_{PIC} = 0$, red curve). The relaxed photoinduced cubic $\text{Mn}^{\text{III}}\text{Fe}^{\text{II}}$ phase is then persistent at room temperature, due to the energy barrier with the initial tetragonal $\text{Mn}^{\text{III}}\text{Fe}^{\text{II}}$ phase, matching the HT phase (red curve).

time-resolved measurements discussed above, which bring key information on the mechanism behind macroscopic and ultrafast PIPT within the thermal hysteresis. The photoinduced $\text{Mn}^{\text{III}}\text{Fe}^{\text{II}}$ CT polarons, forming within 200 fs and living up to 10 μs ³⁴, are sources of anisotropic elastic deformation waves, which propagate at the crystal scale and equilibrate with the lattice on the elastic timescale (100 ps). Compared to the initial LT volume strain v_s , the volume strain v_s^* of the photoexcited lattice is modified by the small polarons resulting from photoinduced CT (Δq) and responsible for volume expansion Δv :

$$v_s^* = v_s + \Delta v \quad (4)$$

The associated photoinduced volume expansion destabilizes the tetragonal lattice, through the elastic coupling cost term $\Delta v \eta^2 > 0$ (with $\Delta v > 0$). Figure 4a depicts the mechanism at play in the transient

polaronic regime at low fluence: the weak volume expansion δv reduces the ferroelastic distortion in the transiently equilibrated PT state ($\eta_{PT} < \eta_{LT}$), which remains tetragonal due to the energy barrier towards the cubic phase. As the photoinduced CT polarons decay within 10 μs , the system relaxes back to the ground LT state with initial volume strain v_s and ferroelastic distortion η_{LT} . In the persistent PIPT regime above threshold fluence (Fig. 4b), the high laser fluence induces larger volume expansion ΔV and therefore larger elastic coupling cost ($\Delta V \eta^2$), that fully destabilizes the tetragonal lattice. As a result, full conversion towards the high-volume cubic symmetry ($\eta = 0$) occurs within the elastic timescale. The system then relaxes towards the equilibrium $\text{Mn}^{\text{III}}\text{Fe}^{\text{II}}$ cubic phase, corresponding to the HT phase. As the energy barrier with the tetragonal $\text{Mn}^{\text{III}}\text{Fe}^{\text{II}}$ phase appears anew after global relaxation, this photoinduced HT phase is persistent at room temperature, and more generally over the wide thermal hysteretic regime of bistability.

The present results demonstrate the possibility to induce by a single laser shot an ultrafast PIPT at room temperature, in a functional material designed to exhibit a wide regime of thermal bistability. Compared to previous single laser shot photoswitching, observed in another RbMnFe derivative at low temperature by static X-ray diffraction studies⁶⁷, our time-resolved analysis also brings key information on the out-of-equilibrium structural and symmetry dynamics. Indeed, these long-range structural reorganizations can only be directly monitored by ultrafast diffraction techniques. The cooperative tetragonal $\text{Mn}^{\text{II}}\text{Fe}^{\text{II}} \rightarrow$ cubic $\text{Mn}^{\text{II}}\text{Fe}^{\text{III}}$ photoinduced phase transition, which occurs above threshold excitation fluence, is persistent and is driven by elastic cooperativity. The energy barrier in the thermodynamic potential between the tetragonal $\text{Mn}^{\text{II}}\text{Fe}^{\text{II}}$ and cubic $\text{Mn}^{\text{II}}\text{Fe}^{\text{III}}$ phases has two important roles. On the one hand, it is responsible for the threshold fluence necessary to induce the cubic phase, as a critical volume expansion is required to destabilize the tetragonal lattice. On the other hand, this volume expansion stabilizes the photoinduced cubic $\text{Mn}^{\text{II}}\text{Fe}^{\text{III}}$ phase, which is persistent over a wide range of bistability. The streaming powder diffraction set-up that we developed made it possible to track structural dynamics at microscopic (Mn–N bonds) and macroscopic (lattice parameters) scales through the non-reversible symmetry and volume changes associated with the photoinduced tetragonal $\text{Mn}^{\text{II}}\text{Fe}^{\text{II}} \rightarrow$ cubic $\text{Mn}^{\text{II}}\text{Fe}^{\text{III}}$ phase transition. Such ultrafast photo-induced phase transitions induced by a single laser pulse are very promising for optically-driven devices, memories, or actuators exhibiting room temperature switching within a wide thermal regime of bistability between states that can persist long after stimuli. As the streaming powder technique can be easily implemented at X-ray free-electron laser beamlines for femtosecond X-ray studies, we also foresee a broad range of applications to study out-of-equilibrium dynamics for non-reversible phenomena in various functional materials^{6,46}.

Methods

Synthesis and characterization of $\text{RbMn}_{0.94}\text{Co}_{0.06}\text{Fe}$

The $\text{Rb}_{0.94}\text{Co}_{0.06}\text{Mn}_{0.94}[\text{Fe}(\text{CN})_6]_{0.98} \cdot 0.2\text{H}_2\text{O}$ material was synthesized and characterized by various techniques (Supplementary Methods 1). The crystals are plate-shaped, with good crystallinity and average size of $0.9 \pm 0.3 \mu\text{m}$. Magnetic measurements indicate that the compound exhibits a thermal phase transition between the HT and LT phases with transition temperatures $T_{\downarrow} = 253 \text{ K}$ and $T_{\uparrow} = 328 \text{ K}$. The XRD powder patterns at room temperature and Rietveld analysis correspond for the HT phase to a cubic space group (F43m) with a lattice constant of $a_{\text{HT}} = 10.5495(6) \text{ \AA}$ and for the LT phase to a tetragonal space group (F42m) with $a_{\text{LT}} = b_{\text{LT}} = 10.0051(11) \text{ \AA}$ and $c_{\text{LT}} = 10.4744(16) \text{ \AA}$. CCDC #2259400 (LT) and #2259401 (HT) contain the supplementary crystallographic data for this paper. These data can be obtained free of charge from The Cambridge Crystallographic Data Centre via www.ccdc.cam.ac.uk/data_request/cif.

Static photoinduced measurements on $\text{RbMn}_{0.94}\text{Co}_{0.06}\text{Fe}$ films

$\text{RbMn}_{0.94}\text{Co}_{0.06}\text{Fe}$ in pure ethanol was deposited on a glass substrate and dried to obtain films of the material (Fig. 1a). Films were cooled below 180 K to reach the $\text{Mn}^{\text{II}}\text{Fe}^{\text{II}}$ LT phase and warmed above 350 K to reach the $\text{Mn}^{\text{II}}\text{Fe}^{\text{III}}$ HT phase. A 532 nm CW laser (FSDL-532-100T, Frankfurt Laser Company) with 100 mW output power was used to photoexcite during 3 s the LT phase at room temperature ($0.5 \times 0.45 \text{ mm}^2$ spot size (FWHM) at the film position, power density of 120 W cm^{-2}) to photoinduce the HT phase. For Fig. 1a, photos were taken with a camera, in the following order and for the same thin film: crystal deposition and cooling at 180 K, photo of the LT phase at room temperature, laser irradiation and photo of the irradiated film at room temperature, heating to 350 K and photo of the heated film.

Setup for streaming powder diffraction

Time-resolved X-ray diffraction (TR-XRD) measurements were performed on time-resolved beamline ID09 at the European Synchrotron Radiation Facility (ESRF)⁵³. The experiment was performed while the ESRF storage ring was operated in 7/8 + 1 filling mode with a single bunch current of 4 mA, corresponding to an X-ray pulse duration of $\sim 35 \text{ ps}$ (HWHM). The X-ray central energy was 14.963 keV ($\lambda = 0.824 \text{ \AA}$, 2% bandwidth), and the beam was focused to a spot size of $25 \times 25 \mu\text{m}^2$ at the sample position. To perform laser pump–X-ray probe measurements, isolated X-ray pulses are synchronized with a 1 ps laser, whose spot size was $210 \mu\text{m} \times 250 \mu\text{m}$. The larger laser spot size ensures a homogeneous excitation of the sample in the volume probed by the X-rays. The laser wavelength was set to 650 nm, exciting crystals on the red edge of their absorption spectrum, which results in a penetration depth of about $1.9 \mu\text{m}$ ⁵⁴, larger than the average size of the crystals ($0.9 \pm 0.3 \mu\text{m}$). Additionally, we studied how photo-response changes with laser fluence, which varied between 0 and 150 mJ cm^{-2} .

For the present streaming powder diffraction study (Supplementary Methods 2–4), crystals of $\text{RbMn}_{0.94}\text{Co}_{0.06}\text{Fe}$ were dispersed in ethanol and streamed through a free-flowing liquid jet to interact with laser and X-ray pulses. The jet size was $300 \mu\text{m}$, and the crystal-solvent weight ratio was 1:270, which corresponds to ~ 500 crystals per shot in the X-ray focus. The flow rate of the jet was set to 1.2 L h^{-1} (jet velocity of 5 m s^{-1} at the interaction region). As a consequence, a fresh ensemble of crystals, which was not excited by previous laser shots, is interacting with the laser pump–X-ray probe beams. The chosen flow rate limits the observation time window to $10 \mu\text{s}$ for pump-probe measurements. Jet was circulated in closed loop, and a cooling device was inserted in the liquid circulation loop in order to compensate for the non-reversible photo-conversion of the already-excited crystals (Supplementary Methods 2). X-ray diffraction patterns were recorded in transmission geometry using a Rayonix MX170-HS CCD detector with an integration time of 5 s for each image. The delay between the laser pump pulse and the X-ray probe pulse was varied from -3 ns to $+10 \mu\text{s}$, and we typically collected 20 diffraction images for each delay. As crystals are randomly oriented in the liquid jet, diffraction images consisted of rings that were azimuthally integrated using pyFAI⁶⁸. We normalized each image over the Q -range of $[5.5; 6.0] \text{ \AA}^{-1}$, where the diffraction signal remains constant along the dynamics.

XRD analysis

The X-ray scattering patterns of $\text{RbMn}_{0.94}\text{Co}_{0.06}\text{Fe}$ were obtained by subtracting the background scattering from the solvent. This was done by subtracting the pattern of pure ethanol, followed by polynomial fitting of residual background (Supplementary Methods 3 and 4). Rietveld refinement of the X-ray diffraction data was performed using TOPAS-Academic version 6 software⁶⁹, with a fixed wavelength of $0.827389 \text{ \AA}^{-1}$ (15 keV as calibrated at the ID09 ESRF beamline). For pure LT and HT phases, refinement was done over the scattering vector Q -range $[0.9; 5.0] \text{ \AA}^{-1}$ using the structures found from powder diffraction, and including refinement of lattice parameters and isotropic Debye–Waller thermal factors. Given the symmetry change between tetragonal LT phase and cubic HT phase, refinement was done considering space group F42m for LT phase and F43m for HT phase in order to directly compare both phases, as explained in our recent work³⁸. Sometimes a weak contribution from HT phase was observed in the equilibrium X-ray diffraction data. Analysis of time-resolved and fluence-dependent diffraction patterns was performed following the same procedure as for pure phases. Background subtraction and Rietveld refinement were performed at each delay. More details are provided in Supplementary Methods 3 and 4.

Data availability

Raw data generated in this study and codes used to process the data have been deposited on the Zenodo repository⁷⁰ under <https://doi.org/10.5281/zenodo.10227842>. Any additional information is available from the corresponding authors upon reasonable request.

References

- Basov, D. N., Averitt, R. D. & Hsieh, D. Towards properties on demand in quantum materials. *Nat. Mater.* **16**, 1077 (2017).
- Fleming, G. R. Concluding remarks: directing and controlling materials and molecules. *Faraday Discuss.* **237**, 419–427 (2022).
- Johnson, S. L. Spiers memorial lecture: from optical to THz control of materials. *Faraday Discuss.* **237**, 9–26 (2022).
- Koshihara, S. et al. Challenges for developing photo-induced phase transition (PIPT) systems: from classical (incoherent) to quantum (coherent) control of PIPT dynamics. *Phys. Rep.* **942**, 1–61 (2022).
- Kirschner, M. S. et al. Photoinduced, reversible phase transitions in all-inorganic perovskite nanocrystals. *Nat. Commun.* **10**, 504 (2019).
- Mariette, C. et al. Strain wave pathway to semiconductor-to-metal transition revealed by time-resolved X-ray powder diffraction. *Nat. Commun.* **12**, 1239 (2021).
- Yue, X. et al. Real-time observation of the buildup of polaron in alpha-FAPbI₃. *Nat. Commun.* **14**, 917 (2023).
- Smit, B. et al. Ultrafast pathways of the photoinduced insulator–metal transition in a low-dimensional organic conductor. *Adv. Mater.* **31**, 1900652 (2019).
- Liu, Q. M. et al. Photoinduced multistage phase transitions in Ta(2)NiSe(5). *Nat. Commun.* **12**, 2050 (2021).
- Bonhommeau, S. et al. One shot laser pulse induced reversible spin transition in the spin-crossover complex [Fe(C₄H₄N₂)₂{Pt(CN)₄}] at room temperature. *Angew. Chem. Int. Ed. Engl.* **44**, 4069–4073 (2005).
- Teitelbaum, S. W. et al. Real-time observation of a coherent lattice transformation into a high-symmetry phase. *Phys. Rev. X* **8**, 031081 (2018).
- Gao, M. et al. Mapping molecular motions leading to charge delocalization with ultrabright electrons. *Nature* **496**, 343–346 (2013).
- Collet, E. et al. Laser-induced ferroelectric structural order in an organic charge-transfer crystal. *Science* **300**, 612–615 (2003).
- Ishikawa, T. et al. Large and ultrafast photoinduced reflectivity change in the charge separated phase of Et₂Me₂Sb[Pd(1,3-dithiol-2-thione-4,5-dithiolate)₂]₂. *Phys. Rev. B* **80**, 115108 (2009).
- Halcrow, M. A. *Spin-crossover Materials: Properties and Applications* (John Wiley & Sons, Ltd, 2013).
- Collet, E. et al. Aperiodic spin state ordering of bistable molecules and its photoinduced erasing. *Phys. Rev. Lett.* **109**, 257206 (2012).
- Ridier, K. et al. Finite size effects on the switching dynamics of spin-crossover thin films photoexcited by a femtosecond laser pulse. *Adv. Mater.* **31**, 1901361 (2019).
- Hoffmann, A., Reznik, D. & Schuller, I. K. Persistent photoinduced effects in high-T_c superconductors. *Adv. Mater.* **9**, 271–273 (1997).
- Schaniel, D. et al. Photoinduced nitrosyl linkage isomers uncover a variety of unconventional photorefractive media. *Adv. Mater.* **19**, 723–726 (2007).
- Xue, J. et al. Photon-induced reversible phase transition in CsPbBr₃ Perovskite. *Adv. Funct. Mater.* **29**, 1807922 (2019).
- Verdaguer, M. et al. Molecules to build solids: high TC molecule-based magnets by design and recent revival of cyano complexes chemistry. *Coord. Chem. Rev.* **190–192**, 1023–1047 (1999).
- Liu, H. W. et al. Reversible valence tautomerism induced by a single-shot laser pulse in a cobalt–iron Prussian blue analog. *Phys. Rev. Lett.* **90**, 167403 (2003).
- Tokoro, H. & Ohkoshi, S. Multifunctional material: bistable metal–cyanide polymer of rubidium manganese hexacyanoferrate. *Bull. Chem. Soc. Jpn.* **88**, 227–239 (2015).
- Zhang, K. et al. Charge-transfer phase transition of a cyanide-bridged Fe(II)/Fe(III) coordination polymer. *Angew. Chem. Int. Ed. Engl.* **55**, 6047–6050 (2016).
- Sato, O., Iyoda, T., Fujishima, A. & Hashimoto, K. Photoinduced magnetization of a cobalt–iron cyanide. *Science* **272**, 704–705 (1996).
- Volatron, F. et al. Photo-induced magnetic bistability in a controlled assembly of anisotropic coordination nanoparticles. *Chem. Commun.* **47**, 1985–1987, (2011).
- Dumont, M. F. et al. Photoinduced magnetism in core/shell Prussian blue analogue heterostructures of K₂Ni[Cr(CN)₆]_n·nH₂O with Rb₂Cob[Fe(CN)₆]_c·mH₂O. *Inorg. Chem.* **50**, 4295–4300 (2011).
- Ohkoshi, S. et al. 90-degree optical switching of output second-harmonic light in chiral photomagnet. *Nat. Photonics* **8**, 65–71 (2014).
- Ohkoshi, S., Imoto, K., Tsunobuchi, Y., Takano, S. & Tokoro, H. Light-induced spin-crossover magnet. *Nat. Chem.* **3**, 564–569 (2011).
- Tokoro, H. et al. Visible-light-induced reversible photomagnetism in rubidium manganese hexacyanoferrate. *Chem. Mater.* **20**, 423–428 (2008).
- Aguila, D., Prado, Y., Koumoussi, E. S., Mathoniere, C. & Clerac, R. Switchable Fe/Co Prussian blue networks and molecular analogues. *Chem. Soc. Rev.* **45**, 203–224 (2016).
- Cammarata, M. et al. Charge transfer driven by ultrafast spin transition in a CoFe Prussian blue analogue. *Nat. Chem.* **13**, 10–14 (2021).
- Azzolina, G. et al. Out-of-equilibrium lattice response to photo-induced charge-transfer in a MnFe Prussian blue analogue. *J. Mater. Chem. C* **9**, 6773–6780 (2021).
- Azzolina, G. et al. Exploring ultrafast photoswitching pathways in RbMnFe Prussian Blue analogue. *Angew. Chem. Int. Ed.* **60**, 23267–23273 (2021).
- Barlow, K. & Johansson, J. O. Ultrafast photoinduced dynamics in Prussian blue analogues. *Phys. Chem. Chem. Phys.* **23**, 8118–8131 (2021).
- Johansson, J. O. et al. Directly probing spin dynamics in a molecular magnet with femtosecond time-resolution. *Chem. Sci.* **7**, 7061–7067 (2016).
- Ohkoshi, S. & Tokoro, H. Photomagnetism in cyano-bridged bimetal assemblies. *Acc. Chem. Res.* **45**, 1749–1758 (2012).
- Azzolina, G. et al. Landau theory for non-symmetry-breaking electronic instability coupled to symmetry-breaking order parameter applied to Prussian blue analog. *Phys. Rev. B* **102**, 134104 (2020).
- Arnett, D. C., Voehringer, P. & Scherer, N. F. Excitation dephasing, product formation, and vibrational coherence in an intervalence charge-transfer reaction. *J. Am. Chem. Soc.* **117**, 12262–12272 (1995).
- Weidinger, D., Brown, D. J. & Owrutsky, J. C. Transient absorption studies of vibrational relaxation and photophysics of Prussian blue and ruthenium purple nanoparticles. *J. Chem. Phys.* **134**, 124510 (2011).
- Moritomo, Y. et al. Photoinduced phase transition into a hidden phase in cobalt hexacyanoferrate as investigated by time-resolved X-ray absorption fine structure. *J. Phys. Soc. Jpn.* **82**, 033601 (2013).
- Zerdane, S. et al. Out-of-equilibrium dynamics driven by photo-induced charge transfer in CsCoFe Prussian blue analogue nanocrystals. *Faraday Discuss.* **237**, 224–236 (2022).
- Asahara, A. et al. Ultrafast dynamics of reversible photoinduced phase transitions in rubidium manganese hexacyanoferrate investigated by midinfrared CN vibration spectroscopy. *Phys. Rev. B* **86**, 195138 (2012).

44. Johnson, S. L. et al. Non-equilibrium phonon dynamics studied by grazing-incidence femtosecond X-ray crystallography. *Acta Crystallogr. Sect. A* **66**, 157–167 (2010).
45. Beaud, P. et al. A time-dependent order parameter for ultrafast photoinduced phase transitions. *Nat. Mater.* **13**, 923–927 (2014).
46. Chergui, M. & Collet, E. Photoinduced structural dynamics of molecular systems mapped by time-resolved X-ray methods. *Chem. Rev.* **117**, 11025–11065 (2017).
47. Ichikawa, H. et al. Transient photoinduced ‘hidden’ phase in a manganite. *Nat. Mater.* **10**, 101–105 (2011).
48. Elsaesser, T. & Woerner, M. Perspective: structural dynamics in condensed matter mapped by femtosecond x-ray diffraction. *J. Chem. Phys.* **140**, 020901 (2014).
49. Yun, J.-H. et al. Early-stage dynamics of chloride ion-pumping rhodopsin revealed by a femtosecond X-ray laser. *Proc. Natl Acad. Sci. USA* **118**, e2020486118 (2021).
50. Coquelle, N. et al. Chromophore twisting in the excited state of a photoswitchable fluorescent protein captured by time-resolved serial femtosecond crystallography. *Nat. Chem.* **10**, 31–37 (2018).
51. Pande, K. et al. Femtosecond structural dynamics drives the trans-cis isomerization in photoactive yellow protein. *Science* **352**, 725–729 (2016).
52. Stockler, L. J. et al. Towards pump-probe single-crystal XFEL refinements for small-unit-cell systems. *IUCRJ* **10**, 103–117 (2023).
53. Cammarata, M. et al. Chopper system for time resolved experiments with synchrotron radiation. *Rev. Sci. Instrum.* **80**, 015101 (2009).
54. Ohkoshi, S., Nuida, T., Matsuda, T., Tokoro, H. & Hashimoto, K. The dielectric constant in a thermal phase transition magnetic material composed of rubidium manganese hexacyanoferrate observed by spectroscopic ellipsometry. *J. Mater. Chem.* **15**, 3291 (2005).
55. Tokoro, H., Nakagawa, K., Imoto, K., Hakoe, F. & Ohkoshi, S. Zero thermal expansion fluid and oriented film based on a bistable metal-cyanide polymer. *Chem. Mater.* **24**, 1324–1330 (2012).
56. Boukheddaden, K. et al. Experimental access to elastic and thermodynamic properties of RbMnFe(CN)₆. *J. Appl. Phys.* **109**, 013520 (2011).
57. Bertoni, R. et al. Elastically driven cooperative response of a molecular material impacted by a laser pulse. *Nat. Mater.* **15**, 606–610 (2016).
58. Bertoni, R. et al. Temperature dependence of the cooperative out-of-equilibrium elastic switching in a spin-crossover material. *Phys. Chem. Chem. Phys.* **21**, 6606–6612 (2019).
59. Enachescu, C. et al. Theoretical approach for elastically driven cooperative switching of spin-crossover compounds impacted by an ultrashort laser pulse. *Phys. Rev. B* **95**, 224107 (2017).
60. Collet, E., Azzolina, G., Jeftić, J. & Lemée-Cailleau, M.-H. Coupled spin cross-over and ferroelasticity: revisiting the prototype [Fe(ptz)₆](BF₄)₂ material. *Adv. Phys.: X* **8**, 2161936 (2023).
61. Collet, E. & Azzolina, G. Coupling and decoupling of spin crossover and ferroelastic distortion: unsymmetric hysteresis loop, phase diagram, and sequence of phases. *Phys. Rev. Mater.* **5**, 044401 (2021).
62. Salje, E. K. & Carpenter, M. A. Linear-quadratic order parameter coupling and multiferroic phase transitions. *J. Phys. Condens. Matter* **23**, 462202 (2011).
63. Carpenter, M. A., Salje, E. K. H. & Graeme-Barber, A. Spontaneous strain as a determinant of thermodynamic properties for phase transitions in minerals. *Eur. J. Mineral.* **10**, 621–691 (1998).
64. Carpenter, M. A. & Salje, E. K. Elastic anomalies in minerals due to structural phase transitions. *Eur. J. Mineral.* **10**, 693 (1998).
65. Salje, E. K. *Phase Transitions in Ferroelastic and Co-elastic Crystals* (Cambridge University Press, 1991).
66. Chernyshov, D., Bürgi, H.-B., Hostettler, M. & Törnroos, K. W. Landau theory for spin transition and ordering phenomena in Fe(II) compounds. *Phys. Rev. B* **70**, 094116 (2004).
67. Azzolina, G. et al. Single laser shot photoinduced phase transition of rubidium manganese hexacyanoferrate investigated by X-ray diffraction. *Eur. J. Inorg. Chem.* **2019**, 3142–3147 (2019).
68. Ashiotis, G. et al. The fast azimuthal integration Python library: pyFAI. *J. Appl. Crystallogr.* **48**, 510–519 (2015).
69. Coelho, A. TOPAS and TOPAS-Academic: an optimization program integrating computer algebra and crystallographic objects written in C++. *J. Appl. Crystallogr.* **51**, 210–218 (2018).
70. Herve, M. et al. Raw Data and Codes for the Article “Ultrafast and persistent photoinduced phase transition at room temperature monitored by streaming powder diffraction” [Data set]. *Zenedo* <https://doi.org/10.5281/zenodo.10227842> (2023).

Acknowledgements

The authors gratefully acknowledge the Agence Nationale de la Recherche for financial support under grant ANR-19-CE30-0004 ELEC-TROPHONE, ANR-19-CE07-0027 SMAC, ANR-19-CE29-0018 MULTI-CROSS and the European Synchrotron Radiation Facility (ESRF) for provision of synchrotron radiation facilities under proposal number CH-6162. G.P. thanks Région Bretagne for partial Ph.D. funding (ARED PHONONIC). I.C. acknowledges financial support from Région Bretagne under grant SAD. E.C. thanks the University of Rennes and the Fondation Rennes 1 for funding. This work was carried out in the frame of a JST FOREST Programme (JPMJFR213Q), a JSPS Grant-in-Aid for Scientific Research (B) (22H02046), Scientific Research (A) (20H00369), and Yasaki Memorial Foundation for Science and Technology. We are grateful to Yugo Nagane (the University of Tokyo) and Mayuko Tanaka (the University of Tsukuba) for their technical support in synthesizing the sample.

Author contributions

E.C., M.C., H.T. and S.O. conceived and funded the project. M.H., G.P., I.C., C.M., M.L. and Y.W. developed the streaming powder diffraction set-up. H.T., S.A. and S.O. synthesized and characterized the sample. M.H., G.P., E.T., S.Z., I.C., C.M., A.V., M.C., M.L. and E.C. performed the time-resolved X-ray diffraction experiment. M.H., G.P., E.T., C.M., M.C. and E.C. analysed the time-resolved X-ray diffraction data. M.H. and R.G.T.R. studied laser-induced sample colour change. M.H. and E.C. set the physical picture with the Landau model. E.C. and M.H. wrote the paper, with contributions from all the authors. All authors have approved the final version of the paper.

Competing interests

The authors declare no competing interests.

Additional information

Supplementary information The online version contains supplementary material available at <https://doi.org/10.1038/s41467-023-44440-3>.

Correspondence and requests for materials should be addressed to Hiroko Tokoro, Shin-ichi Ohkoshi or Eric Collet.

Peer review information *Nature Communications* thanks the anonymous reviewers for their contribution to the peer review of this work. A peer review file is available.

Reprints and permissions information is available at <http://www.nature.com/reprints>

Publisher’s note Springer Nature remains neutral with regard to jurisdictional claims in published maps and institutional affiliations.

Open Access This article is licensed under a Creative Commons Attribution 4.0 International License, which permits use, sharing, adaptation, distribution and reproduction in any medium or format, as long as you give appropriate credit to the original author(s) and the source, provide a link to the Creative Commons license, and indicate if changes were made. The images or other third party material in this article are included in the article's Creative Commons license, unless indicated otherwise in a credit line to the material. If material is not included in the article's Creative Commons license and your intended use is not permitted by statutory regulation or exceeds the permitted use, you will need to obtain permission directly from the copyright holder. To view a copy of this license, visit <http://creativecommons.org/licenses/by/4.0/>.

© The Author(s) 2024